Biophysical Journal
Article

Biophysical Society

Target Membrane Cholesterol Modulates Single Influenza Virus Membrane Fusion Efficiency but Not Rate

Katherine N. Liu[1] and Steven G. Boxer[1,*]
[1]Department of Chemistry, Stanford University, Stanford, California

ABSTRACT Host lipid composition influences many stages of the influenza A virus (IAV) entry process, including initial binding of IAV to sialylated glycans, fusion between the viral envelope and the host membrane, and the formation of a fusion pore through which the viral genome is transferred into a target cell. In particular, target membrane cholesterol has been shown to preferentially associate with virus receptors and alter physical properties of the membrane like fluidity and curvature. These properties affect both IAV binding and fusion, which makes it difficult to isolate the role of cholesterol in IAV fusion from receptor binding effects. Here, we develop a fusion assay that uses synthetic DNA-lipid conjugates as surrogate viral receptors to tether virions to target vesicles. To avoid the possibly perturbative effect of adding a self-quenched concentration of dye-labeled lipids to the viral membrane, we tether virions to lipid-labeled target vesicles and use fluorescence microscopy to detect individual, pH-triggered IAV membrane fusion events. Through this approach, we find that cholesterol in the target membrane enhances the efficiency of single-particle IAV lipid mixing, whereas the rate of lipid mixing is independent of cholesterol composition. We also find that the single-particle kinetics of influenza lipid mixing to target membranes with different cholesterol compositions is independent of receptor binding, suggesting that cholesterol-mediated spatial clustering of viral receptors within the target membrane does not significantly affect IAV hemifusion. These results are consistent with the hypothesis that target membrane cholesterol increases lipid mixing efficiency by altering host membrane curvature.

SIGNIFICANCE Influenza A virus is responsible for millions of cases of the flu each year. In order to replicate, influenza must enter a host cell through virus membrane fusion, and cholesterol in the target membrane is vital to the dynamics of this process. We report a receptor-free, single-virus fusion assay that requires no fluorescent labeling of virus particles. We use this assay to show that cholesterol increases the fraction of fusion events in a manner that is correlated with the spontaneous curvature of the target membrane but is independent of receptor binding. This assay represents a promising strategy for studying the viral fusion processes of other enveloped viruses.

INTRODUCTION

For influenza A virus (IAV) to replicate, hemagglutinin (HA), a viral envelope protein, must first bind to negatively-charged sialylated glycolipids or glycoproteins on the host plasma membrane. Once IAV is bound and endocytosed, viral content entry is facilitated by membrane fusion, in which endosomal low pH triggers a conformational rearrangement of HA, and the membranes of IAV and the target cell mix to form a hemifusion intermediate (1,2). Lipid mixing is followed by the formation of a fusion pore, through which the viral genome is transferred into the target cell (3,4).

Host membrane composition influences each stage of the IAV entry process, though it is not entirely clear how it does so on a molecular scale (5,6). Target membrane cholesterol has been shown to cluster with sialic acid-presenting glycolipids, which increases IAV binding avidity (7). It has also been demonstrated in bulk studies that cholesterol in target vesicles speeds the rates of IAV hemifusion and fusion pore formation (8), which may be facilitated by the negative spontaneous curvature (SC) of cholesterol (9). For other enveloped viruses like human immunodeficiency virus, fusion peptide insertion is facilitated by cholesterol in the target membrane, which has led to speculation that cholesterol

Submitted December 19, 2019, and accepted for publication March 23, 2020.

*Correspondence: sboxer@stanford.edu

Editor: Claudia Steinem.
https://doi.org/10.1016/j.bpj.2020.03.021

may play some role in facilitating HA engagement for IAV (10–12). Given that cholesterol may stabilize each fusion intermediate (5), bulk measurements cannot deconvolve the mechanistic details of cholesterol's influence on IAV fusion.

Single-particle virus lipid mixing techniques have enabled researchers to separate the dynamics of virion binding from subsequent steps in IAV membrane fusion (13). These approaches typically utilize fluorescence microscopy and dequenching to monitor receptor-bound individual virions fusing to artificial membrane bilayers (14–16). Models and simulations based on experimental kinetics have shown that lipid mixing is the rate-limiting step of IAV membrane fusion (17,18). It is postulated that a minimum of three neighboring HA trimers must engage in the target membrane to yield a productive hemifusion event (17,19). This estimate suggests that clustering of HAs, as a result of receptor binding and possibly mediated or affected by membrane composition, could enhance the rate of IAV fusion.

It has been difficult to isolate the role of receptor binding in IAV fusion because HA is responsible for both IAV binding and fusing to the host membrane. To disentangle receptor binding and fusion, our lab previously developed a single-particle assay that uses synthetic DNA-lipid surrogate receptors and lipid dequenching assays to observe lipid mixing (hemifusion) between single virions and surface-tethered vesicles (Fig. S1 *A*; (20,21)). Application of this assay demonstrated that kinetics of IAV lipid mixing to target membranes containing 10 mol % cholesterol are the same when virus and vesicle are tethered through DNA-lipid surrogates or GD1a sialic acid receptors (20).

Despite the fact that single-particle approaches have yielded an immense amount of kinetic information about IAV fusion, a limitation of currently existing strategies is that they all involve introducing a self-quenched concentration of fluorescently tagged lipids to the viral envelope and/or fluorescent dye to the viral content. The labeling process exposes virions to organic solvents like ethanol and dimethyl sulfoxide, which can potentially impact virus infectivity. At self-quenched concentrations, unnatural fluorescent lipids comprise roughly 3–5 mol % of the IAV envelope, and this has been shown to affect the observed lipid mixing kinetics of IAV fusion (22).

In this study, we introduce an assay architecture to observe single-particle virus lipid mixing events, illustrated in Fig. 1 (compare with Fig. S1 *A*), that limits the fluorescent label to the target vesicle, thereby avoiding the perturbative process of adding fluorescent dye to viruses. This assay minimizes changes to the virus envelope composition, which enables the study of viral entry dynamics of virions that more closely resemble a native population. As in our previous assay, this approach utilizes sequence-specific DNA-lipid conjugates to tether IAV to target membranes in the absence of the native sialic acid viral receptor. We apply this strategy to study the impact of target membrane cholesterol on IAV lipid mixing kinetics at the single-particle level. By varying the amount of cholesterol in target membranes from 10 to 40 mol %, we show that although cholesterol enhances the efficiency or fraction of productive IAV lipid mixing events, the rate of fusion is independent of target membrane composition in both the presence and absence of the native viral receptor GD1a. This suggests that cholesterol-mediated spatial clustering of viral receptors in the target membrane does not have a significant impact on the rate-limiting step of IAV lipid mixing. Additionally, we relate the cholesterol dependence of IAV lipid mixing efficiency to the SC of the target membrane.

MATERIALS AND METHODS

Materials

Palmitoyl oleoyl phosphatidylcholine (POPC), dioleoyl phosphatidylethanolamine (DOPE), and cholesterol were purchased from Avanti Polar Lipids (Alabaster, AL). Texas Red 1,2-dihexadecanoyl-*sn*-glycero-3-phosphoethanolamine (TR-DHPE), Oregon Green 1,2-dihexadecanoyl-*sn*-glycero-3-phosphoethanolamine (OG-DHPE), fatty-acid-depleted bovine serum albumin (BSA), and NeutrAvidin were purchased from Thermo

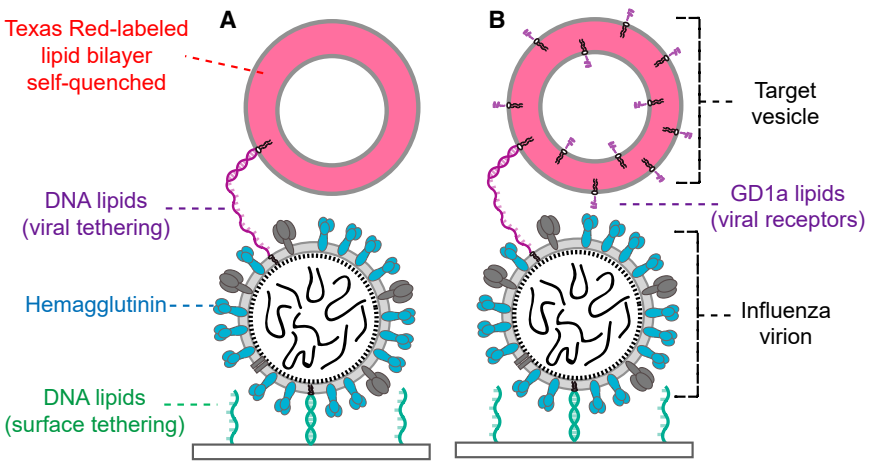

FIGURE 1 Schematic of influenza A virions bound to Texas Red lipid-labeled target vesicles. Vesicles (*red*) are bound to virions by (*A*) hybridization of complementary sequences of membrane-anchored DNA (*purple*) or (*B*) both membrane-anchored DNA and GD1a glycolipid receptors (*black*). GD1a binds to viral HA (*blue*). In both architectures, the substrate displays single-stranded DNA (*green*). Virions are surface tethered by DNA hybridization with a membrane-anchored antisense DNA sequence (*green*) that is orthogonal to the sequence used for viral tethering (*purple*). Details of surface functionalization are not shown (see Supporting Materials and Methods); the schematic is not drawn to scale. To see this figure in color, go online.

Fisher Scientific (Waltham, MA). Disialoganglioside GD1a from bovine brain (Cer-Glc-Gal(NeuAc)-GalNAc-Gal-NeuAc) was purchased from Sigma-Aldrich (St. Louis, MO). Chloroform, methanol, and buffer salts were obtained from Fisher Scientific (Pittsburgh, PA) and Sigma-Aldrich. Polydimethylsiloxane was obtained from Ellsworth Adhesives (Hayward, CA). Poly(L-lysine)-graft-poly(ethylene glycol) (PLL-g-PEG) and PLL-g-PEG biotin were purchased from SuSoS (Dübendorf, Switzerland).

Buffers

The following buffers were used: vesicle buffer (10 mM NaH_2PO_4, 90 mM sodium citrate, and 150 mM NaCl (pH 7.4)), fusion buffer (10 mM NaH_2PO_4, 90 mM sodium citrate, and 150 mM NaCl (pH 5.1)), and HB buffer (20 mM HEPES and 150 mM NaCl (pH 7.2)).

Microscopy

Epifluorescence micrographs were acquired with a Nikon Ti-U microscope using a 100× oil immersion objective, NA = 1.49 (Nikon Instruments, Melville, NY), a Spectra-X LED Light Engine (Lumencor, Beaverton, OR) for illumination, and an Andor iXon 897 EMCCD camera (Andor Technologies, Belfast, UK) with 16-bit image settings. Images were captured with MetaMorph software (Molecular Devices, Sunnyvale, CA). See Supporting Materials and Methods for additional microscopy information.

DNA-lipid and biotin-DNA preparation

DNA lipids (see Table S1 for sequences) used to surface tether viruses and tether target vesicles to viruses were synthesized as previously described (23). Biotin DNA was synthesized by the Protein and Nucleic Acid Facility at Stanford University and diluted to the desired concentration in deionized water. All DNA oligos were stored at −20°C.

Vesicle preparation

Lipid mixtures were prepared in chloroform and dried down to a film under argon gas, and the film was dried under house vacuum for at least 3 h. Mixtures contained 20 mol % DOPE, 10–40 mol % cholesterol, 7 mol % TR-DHPE, 0 or 2 mol % GD1a, and the remaining mol % POPC (see Table S1). Dried lipid films were resuspended in vesicle buffer (10 mM NaH_2PO_4, 90 mM sodium citrate, and 150 mM NaCl (pH 7.4)) by vortexing, and large unilamellar vesicles with a nominal diameter of 100 nm were prepared by extrusion. We note that recent evidence has shown that extrusion yields a fraction of vesicles that are multilamellar (24), although not under our preparation conditions. This would likely not affect lipid mixing measurements, but it could potentially impact measurements of content mixing. Vesicle suspensions were stored at 4°C and used within a week. To incorporate DNA lipids into the outer leaflet of vesicles, DNA lipids were added to a vesicle suspension and incubated overnight at 4°C, as described in a previous study (20).

Influenza virus preparation

IAV (strain X-31, A/Aichi/68, H3N2) was purchased from Charles River Laboratories (Wilmington, MA). Virus was pelleted in HB buffer by centrifugation at 21,130 rcf for 50 min and resuspended in 100 μL of fresh HB buffer. DNA lipids were incorporated into the IAV envelope by incubating virus sample at 4°C on ice overnight according to a previously described method (20). IAV is a BSL-2 agent and was handled following an approved biosafety protocol at Stanford University.

Surface and architecture preparation

The single-virus lipid mixing architecture was prepared as shown in Fig. 1. In a microfluidic flow cell (see Supporting Materials and Methods for details), glass slides were functionalized by incubating a mixture of 5 μL of a 19:1 mixture of PLL-g-PEG (1 g/L) and PLL-g-PEG biotin (1 g/L) in HB buffer for at least 30 min. Flow cells were rinsed with deionized water and vesicle buffer and stored overnight at 4°C. The following day, 5 μL of NeutrAvidin (1 g/L) was incubated for 15 min. After rinsing away excess NeutrAvidin with vesicle buffer, 2 μL of biotin DNA (178 μM, sequence A; see Table S1 for sequences) was incubated for 20 min. The flow cell was thoroughly rinsed with vesicle buffer to remove excess biotin DNA. Next, 5 μL of IAV in HB buffer (roughly 5.4 nM) displaying sequences A′ (antisense to A) and B was introduced to the flow cell and tethered to the substrate. After rinsing the flow cell with vesicle buffer, the surface was further passivated by incubating it with 10 μL of BSA (1 g/L) for at least 10 min to prevent nonspecific binding of added target vesicles. Finally, 2–3 μL of ∼100-nm-diameter vesicles displaying DNA sequence B′ and/or containing GD1a were introduced (2.8 μM nominal total lipid concentration) and allowed to bind for 5–10 min to control surface density and ensure spatial separation between particles. Excess unbound vesicles were removed by rinsing with vesicle buffer.

Lipid mixing assay

Fluorescence microscopy was used to collect a video micrograph image stream of 1000 frames at a rate of 3.47 frames/s. After the image stream was started, the pH of flow cell was rapidly exchanged from 7.4 to 5.1 using fusion buffer. In a separate experiment, tethered vesicles that contained a pH indicator (2 mol % OG-DHPE) were used to calibrate the exchange time of fusion buffer (2–3 s). The time between the lowering of pH and dequenching was extracted using custom MATLAB (The MathWorks, Natick, MA) scripts, as described previously (20,21). In 0.5% of traces or fewer, more than one dequenching event is observed in the same region, reflecting that more than one vesicle was bound to the same virion or that there was insufficient spatial separation between particles. The wait times from fluorescence traces with more than one dequenching event are excluded from cumulative distribution functions (CDFs).

RESULTS AND DISCUSSION

Single-virus lipid mixing assay

We developed an assay that monitors single lipid mixing events and eliminates the need to fluorescently label virions (assay schematized in Fig. 1). As in our previous strategy, synthetic DNA lipids are used for two purposes: 1) to surface immobilize influenza virions and 2) to tether target vesicles to virions in the presence and absence of sialic acid receptors.

First, DNA lipids with two orthogonal sequences (Fig. 1, *green* and *purple*) are incorporated into the envelope of influenza A virions. This is accomplished by incubating virions with an aqueous suspension of DNA lipids; that is, no organic solvents are used. For each sequence, the median number of DNA lipids incorporated into each virion is seven (Fig. S2). As previously observed, when DNA lipids are incubated with virions or lipid vesicles, DNA-lipid incorporation into the IAV envelope does not follow Poisson statistics (20,25). The median number of DNA-lipids per virion is 200- to 350-fold fewer than

the number of fluorescently tagged lipids added to the viral envelope to achieve a self-quenched concentration in alternate architectures. Virions are added to a microfluidic flow cell containing a carefully passivated substrate. The substrate displays a complementary DNA sequence to one of the DNA-lipid sequences on the virion (*green*), leading to surface immobilization of the virions through DNA hybridization.

After the flow cell is rinsed extensively, BSA is added to further passivate the substrate and prevent nonspecific binding of incoming target vesicles. We stress that effective surface passivation requires optimization to ensure that the target vesicles are specifically bound to virions. Target vesicles containing DNA-lipids are introduced to the flow cell at a dilute concentration and become tethered to virions through hybridization of complementary DNA sequences (*purple*). Vesicles are bound sparsely for sufficient spatial resolution to monitor single events. These target vesicles are lipid labeled with a self-quenched concentration of TR-DHPE (7 mol %). For all lipid mixtures, vesicles are ~100 nm in diameter (Fig. S3) to ensure that mixing and dilution with the viral envelope membrane, which is also ~100 nm in diameter (albeit quite heterogenous (26)), will result in dequenching. In the absence of IAV or sequence-specific DNA tethers, very few vesicles bind to the passivated substrate (Fig. S4). Untethered vesicles are thoroughly rinsed and removed from the flow cell before lowering the pH.

To study lipid mixing kinetics in the presence of sialic acid receptors, target vesicles were also prepared with sialic acid-containing glycolipids (ganglioside GD1a) in addition to DNA lipids. Because of the transient and reversible interaction of IAV with GD1a, DNA lipids are required during preparation of target vesicles to ensure that vesicles remain bound.

Once virions and target vesicles are bound, the pH of the flow cell is lowered from pH 7.4 to 5.1 through rapid buffer exchange. A video micrograph monitoring the Texas-Red signal of vesicles is collected for 1000 frames at 288 ms/frame. The dequenching of TR-DHPE represents lipid transfer from the target vesicle to the IAV envelope (Fig. 2, *A* and *B*). The experimental readout of this assay is limited to lipid mixing. As in previous studies (27), lipid dequenching is interpreted as hemifusion between a virion and target vesicle. Fluorescence traces of individual events are analyzed to extract the time interval from pH drop to lipid mixing (Fig. 2 *C*). Individual wait times are compiled in a CDF (Fig. 3, *A* and *B*). CDFs were used rather than histograms to present wait times because they do not require data to be selectively binned. In the absence of IAV, there are no vesicles that undergo fluorescence dequenching when the pH of the system is lowered (Fig. S5), which indicates that all vesicle dequenching events observed can be attributed to viral lipid mixing. The kinetics of lipid mixing observed with this architecture

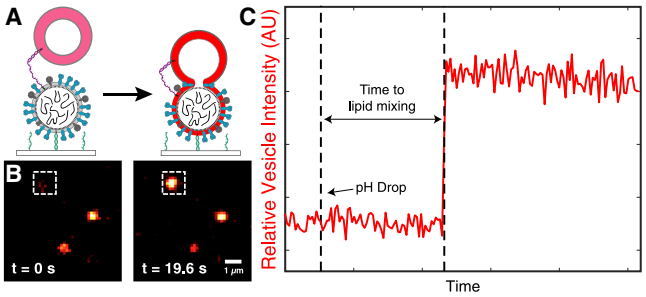

FIGURE 2 Lowering the pH triggers virion-target vesicle lipid mixing detected by fluorescence dequenching. (*A*) Schematic diagram illustrating the single-virus lipid mixing experiment. A Texas-Red-labeled vesicle (self-quenched concentration) is tethered via DNA lipids to a surface-tethered influenza virion (see Fig. 1 *A*). When the pH is lowered, lipid mixing occurs, and the lipids in the target vesicle are diluted upon mixing with the viral membrane. The schematic is not drawn to scale. (*B*) Example microscope images of Texas-Red-labeled vesicles that are bound to surface-tethered influenza virions. At pH 7.4 (*left*), the self-quenched target vesicle is dim but detectable. After the pH is lowered to 5.1 (*right*), particles display dequenching due to lipid mixing. (*C*) Example time trace (*red*) of the fluorescence intensity of a Texas-Red vesicle (shown in *white box* in *B*) that undergoes dequenching. The wait time is defined as the time from the pH drop to the lipid mixing event. To see this figure in color, go online.

are indistinguishable from our previously published single-virus measurements that monitored dequenching of lipid-labeled IAV (Fig. S6; (20)).

Cholesterol enhances the efficiency of IAV lipid mixing but does not alter the rate

To gain mechanistic insight into the role of cholesterol in IAV hemifusion, we performed single-virus lipid mixing experiments on virions that were DNA tethered to target membranes that contained varying mole fractions of cholesterol. The wait times to lipid mixing for each composition were compiled into separate CDFs (Fig. S7) and compared. Surprisingly, from 10 to 40 mol % cholesterol, the rates of IAV lipid mixing are the same within experimental error (Fig. 3 *A*). However, the relative efficiency of lipid mixing, or the fraction of vesicles within a field of view that undergo dequenching, increased four-fold as the target membrane cholesterol composition was increased from 10 to 40 mol % (Fig. 3 *C*). The total number of vesicles analyzed is proportional to the number of individual experiments executed and not because of inherent differences in tethering behavior.

To understand whether cholesterol-mediated GD1a spatial ordering (7) impacts the kinetics of lipid mixing, we introduced GD1a (2 mol %) to target vesicles in addition to DNA-lipids, then varied the mole fraction of cholesterol in the target membrane from 10 to 40 mol %. Similar to IAV lipid mixing with DNA-tethered target membranes, when GD1a is also present in target vesicles, the rates of IAV lipid mixing are independent of the mole fraction of

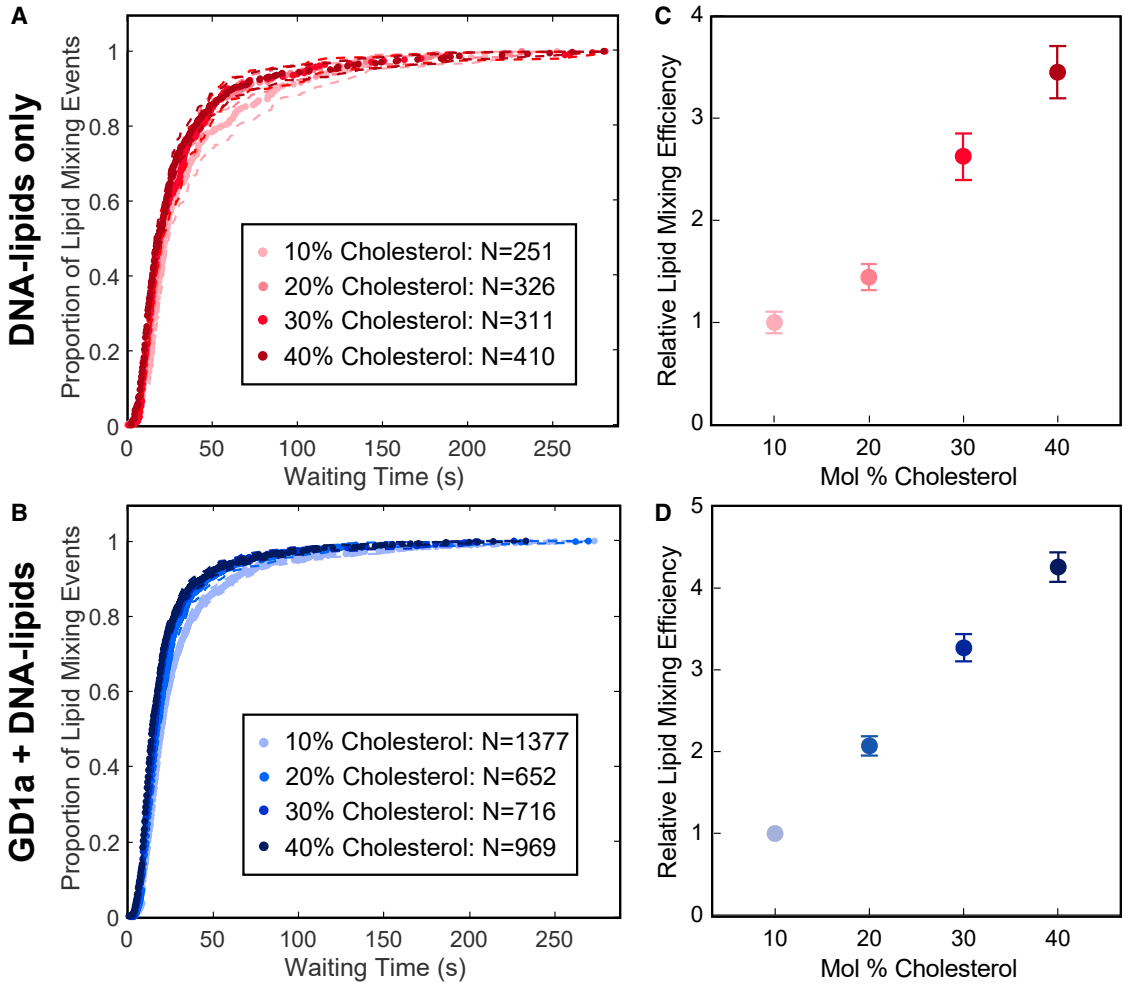

FIGURE 3 Cholesterol enhances the efficiency of single-particle IAV lipid mixing, whereas the rate of lipid mixing is independent of target membrane cholesterol composition. (*A*) Wait times for individual lipid mixing events are plotted as cumulative distribution functions (CDFs). From 10 to 40 mol % cholesterol, the rate of IAV lipid mixing is the same within bootstrap resampling error (95% confidence intervals, *dashed lines*; see Fig. S7 for individual CDFs). (*B*) In the presence of native viral receptor GD1a, the rate of lipid mixing is also unaffected by increasing the ratio of cholesterol in the target membrane within bootstrap resampling error (95% confidence intervals, *dashed lines*). (*C*) The relative efficiency or fraction of target vesicles that undergo dequenching increases four-fold as the mole percentage of cholesterol in DNA-tethered target vesicles increases. For (*C*) and (*D*), the lipid mixing efficiency to membranes containing 10 mol % cholesterol is normalized to 1, and points represent the average efficiency value ± bootstrap resampling error. (*D*) When target membranes contain GD1a, the relative efficiency of lipid mixing also increases four-fold. Kinetic data for each composition were compiled from at least two independent viral preparations. To see this figure in color, go online.

cholesterol in the target membrane (Fig. 3 *B*). Increasing the amount of cholesterol from 10 to 40 mol % also enhances the relative efficiency of IAV lipid mixing by four-fold (Fig. 3 *D*).

Although target vesicles were bound by both GD1a and DNA-lipids, the quantity of GD1a glycolipids is roughly 40-fold greater than the median number of DNA-lipids per vesicle. Because of the large excess of GD1a, we hypothesize that the lipid mixing kinetics observed are primarily influenced by the GD1a-HA interactions between IAV and target vesicle. Additionally, the rates found through the vesicle-labeled architecture in this study are indistinguishable from previous measurements of IAV-labeled, GD1a-mediated lipid mixing (20).

The single-virus lipid mixing data from our study show that whereas cholesterol increases the fraction of productive hemifusion events, the rate of IAV lipid mixing is independent of cholesterol composition. These observations are consistent with the increase in extent of IAV fusion found in bulk ensemble measurements when target membrane cholesterol is increased (8,28). In a different single-particle study, it was found that cholesterol increases both the rate and efficiency of lipid mixing of lipid-labeled influenza virions bound to supported lipid bilayers by GD1a (29). We hypothesize that our results may differ from this observation because of differences in assay architecture and in virion labeling. In supported lipid bilayer architectures, during lipid mixing, the lipids from the viral envelope diffuse into the

target membrane, and as a result, the composition of the target bilayer changes as time progresses, as evidenced by the buildup of the fluorescent background in the supported bilayer. In the tethered vesicle architecture that we employ in this study, each fusion event is confined, and membrane mixing does not influence neighboring events. Furthermore, adding large quantities of octadecyl rhodamine B to the viral envelope has been shown to affect the observed IAV lipid mixing kinetics in single-virus measurements (22).

The close similarity of kinetics of IAV lipid mixing to receptor (GD1a)-containing and receptor-free target membranes (traces overlaid in Fig. S8) supports our previous finding that the absence of GD1a does not impact the spatial organization of viral HA in a manner that alters the kinetics of lipid mixing (20). This study further demonstrates that lipid mixing kinetics are independent of receptor binding across a range of target membrane lipid compositions. We do not directly measure HA engagement with the target membrane, so at this point, we are unable make any claims about the impact of cholesterol on lipid mixing intermediates. Although cholesterol has been shown to cluster with target receptors (7,30), the concentration of cholesterol in target membranes does not significantly alter the rate-limiting step of IAV fusion.

Cholesterol may stabilize hemifusion to increase IAV lipid mixing efficiency

We sought to understand how cholesterol acts to modulate the physical properties of the target membrane to yield a greater number of productive IAV lipid mixing events. In addition to the fact that cholesterol increases bilayer rigidity and leads to greater orientational order (31), cholesterol generates negative curvature in lipid monolayers, which can promote the formation of highly curved membrane structures. It is well established that the hemifusion stalk formed during vesicle (32) and IAV membrane fusion is stabilized by negative SC (33). Cryo-electron tomography images have shown that increasing cholesterol in the target membrane or modulating SC through lipid composition can induce different hemifusion structures and pathways to IAV fusion (34).

To understand the relationship between lipid mixing efficiency and curvature, we estimated the monolayer SC for each mixture tested in this study using published values for each individual membrane component (Table S2; (35)). Several assumptions were needed to estimate the lipid mixture SC. The calculations assume no asymmetry between the inner and outer leaflets of the target vesicles, although it is important to note that any asymmetry in lipid composition between membrane leaflets can impact the effective membrane SC. The contributions of TR-DHPE and ganglioside GD1a were also omitted. There is no agreed-upon experimental value for the individual contribution of GD1a to membrane SC, although gangliosides like GM1 have been suggested to induce positive curvature (36), and GD1a has been shown to induce high-curvature clusters in phosphatidylethanolamine membranes (37). With these assumptions, for mixtures containing 10, 20, 30, and 40 mol % cholesterol, the estimated SC values were −0.142, −0.190, −0.237, and −0.284 nm^{-1}, respectively.

As shown in Fig. 4, the lipid mixing efficiency values increase as the target membrane SC becomes more negative. The relative efficiencies of lipid mixing increase slightly for virions that are both DNA tethered and bound by GD1a, perhaps because GD1a may additionally induce curvature in these specific lipid mixtures that favorably stabilizes the hemifusion stalk. Another explanation is that in the absence of GD1a, DNA tethering could potentially bind vesicles to a greater proportion of fusion-incompetent virions that are unable to bind to GD1a, therefore decreasing the relative efficiency. These two hypotheses are difficult to test and deconvolve because there is, as of yet, no way to directly characterize each individual virion (and target vesicle) whose kinetics are observed.

Our analysis focuses on the curvature of the hemifusion intermediate formed between IAV and the target membrane. Although the overall curvature of vesicles in this model system differs from the curvature of the endosomal membrane that IAV typically fuses to in a cell, the curvature of the hemifusion stalk in both environments is likely to be similar.

The correlation between target membrane SC and IAV lipid mixing efficiencies suggests that the dominant effect

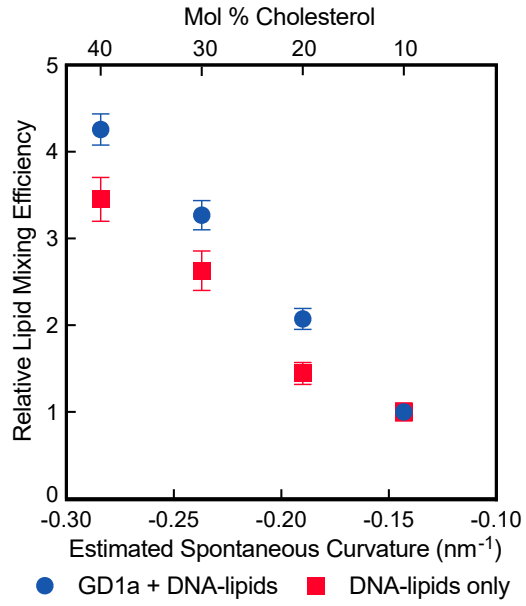

FIGURE 4 IAV lipid mixing efficiency increases when the estimated SC becomes more negative. This trend is observed in both the presence (*blue*) and absence (*red*) of viral ganglioside receptor GD1a. The points represent the average efficiency value ± bootstrap resampling error. To see this figure in color, go online.

of cholesterol in IAV lipid mixing is in facilitating the creation of the hemifusion stalk intermediate. The stabilization of this fusion intermediate enables a greater number of successful lipid mixing events to occur while imparting no significant perturbation on the rate-limiting step of IAV fusion.

CONCLUSIONS

We have presented a strategy to observe single-virus lipid mixing events that eliminates the need to add high concentrations of fluorescently-tagged lipids to the viral envelope. Using this approach, we find that the rate of IAV lipid mixing is insensitive to the mole fraction of cholesterol in the target membrane, whereas the efficiency is enhanced in a manner that is correlated with the SC of the target membrane. We also show that nanoscale clustering of GD1a and cholesterol in the target membrane does not have a significant impact on either the rate or relative efficiency of IAV lipid mixing in a manner that can be detected in this assay.

Although this study only reports lipid mixing of IAV, the general strategy of restricting fluorescent labels to the target vesicle is promising for observing other viral processes, in particular content mixing, and this will be reported separately. This general architecture could also be adapted to observe target membrane fusion kinetics of other enveloped viruses, especially for viral samples that require harsh conditions to fluorescently label or in which the receptor is either unknown or difficult to work with.

SUPPORTING MATERIAL

Supporting Material can be found online at https://doi.org/10.1016/j.bpj.2020.03.021.

AUTHOR CONTRIBUTIONS

K.N.L. designed experiments, performed experiments, analyzed data, and co-wrote the article. S.G.B. designed experiments and co-wrote the article.

ACKNOWLEDGMENTS

The authors thank Elizabeth Webster, Prof. Robert Rawle, Prof. Peter Kasson, Steven Tan, and Amani Hariri for helpful discussions.

K.N.L. was supported by a National Science Foundation Graduate Research Fellowship. This work was supported by National Institutes of Health Grant R35 GM118044 to S.G.B. Part of this work was performed at the Stanford Nano Shared Facilities, which is supported by the National Science Foundation under award ECCS-1542152.

REFERENCES

1. Skehel, J. J., and D. C. Wiley. 2000. Receptor binding and membrane fusion in virus entry: the influenza hemagglutinin. *Annu. Rev. Biochem.* 69:531–569.
2. Eckert, D. M., and P. S. Kim. 2001. Mechanisms of viral membrane fusion and its inhibition. *Annu. Rev. Biochem.* 70:777–810.
3. Chernomordik, L. V., E. Leikina, …, J. Zimmerberg. 1999. Structural intermediates in influenza haemagglutinin-mediated fusion. *Mol. Membr. Biol.* 16:33–42.
4. Harrison, S. C. 2015. Viral membrane fusion. *Virology.* 479–480:498–507.
5. Yang, S. T., A. J. B. Kreutzberger, …, L. K. Tamm. 2016. The role of cholesterol in membrane fusion. *Chem. Phys. Lipids.* 199:136–143.
6. Chernomordik, L. V., E. Leikina, …, J. Zimmerberg. 1997. An early stage of membrane fusion mediated by the low pH conformation of influenza hemagglutinin depends upon membrane lipids. *J. Cell Biol.* 136:81–93.
7. Goronzy, I. N., R. J. Rawle, …, P. M. Kasson. 2018. Cholesterol enhances influenza binding avidity by controlling nanoscale receptor clustering. *Chem. Sci. (Camb.).* 9:2340–2347.
8. Domanska, M. K., D. Wrona, and P. M. Kasson. 2013. Multiphasic effects of cholesterol on influenza fusion kinetics reflect multiple mechanistic roles. *Biophys. J.* 105:1383–1387.
9. Churchward, M. A., T. Rogasevskaia, …, J. R. Coorssen. 2008. Specific lipids supply critical negative spontaneous curvature–an essential component of native Ca2+-triggered membrane fusion. *Biophys. J.* 94:3976–3986.
10. Lai, A. L., A. E. Moorthy, …, L. K. Tamm. 2012. Fusion activity of HIV gp41 fusion domain is related to its secondary structure and depth of membrane insertion in a cholesterol-dependent fashion. *J. Mol. Biol.* 418:3–15.
11. Epand, R. M. 2003. Fusion peptides and the mechanism of viral fusion. *Biochim. Biophys. Acta.* 1614:116–121.
12. Meher, G., S. Sinha, …, H. Chakraborty. 2019. Cholesterol modulates membrane properties and the interaction of gp41 fusion peptide to promote membrane fusion. *J. Phys. Chem. B.* 123:7113–7122.
13. Floyd, D. L., J. R. Ragains, …, A. M. van Oijen. 2008. Single-particle kinetics of influenza virus membrane fusion. *Proc. Natl. Acad. Sci. USA.* 105:15382–15387.
14. Wessels, L., M. W. Elting, …, K. Weninger. 2007. Rapid membrane fusion of individual virus particles with supported lipid bilayers. *Biophys. J.* 93:526–538.
15. Costello, D. A., D. W. Lee, …, S. Daniel. 2012. Influenza virus-membrane fusion triggered by proton uncaging for single particle studies of fusion kinetics. *Anal. Chem.* 84:8480–8489.
16. Otterstrom, J. J., B. Brandenburg, …, A. M. van Oijen. 2014. Relating influenza virus membrane fusion kinetics to stoichiometry of neutralizing antibodies at the single-particle level. *Proc. Natl. Acad. Sci. USA.* 111:E5143–E5148.
17. Ivanovic, T., J. L. Choi, …, S. C. Harrison. 2013. Influenza-virus membrane fusion by cooperative fold-back of stochastically induced hemagglutinin intermediates. *eLife.* 2:e00333.
18. Ivanovic, T., and S. C. Harrison. 2015. Distinct functional determinants of influenza hemagglutinin-mediated membrane fusion. *eLife.* 4:e11009.
19. Danieli, T., S. L. Pelletier, …, J. M. White. 1996. Membrane fusion mediated by the influenza virus hemagglutinin requires the concerted action of at least three hemagglutinin trimers. *J. Cell Biol.* 133:559–569.
20. Rawle, R. J., S. G. Boxer, and P. M. Kasson. 2016. Disentangling viral membrane fusion from receptor binding using synthetic DNA-lipid conjugates. *Biophys. J.* 111:123–131.
21. Rawle, R. J., E. R. Webster, …, S. G. Boxer. 2018. pH dependence of Zika membrane fusion kinetics reveals an off-pathway state. *ACS Cent. Sci.* 4:1503–1510.
22. Rawle, R. J., A. M. Villamil Giraldo, …, P. M. Kasson. 2019. Detecting and controlling dye effects in single-virus fusion experiments. *Biophys. J.* 117:445–452.

23. Chan, Y. H., B. van Lengerich, and S. G. Boxer. 2008. Lipid-anchored DNA mediates vesicle fusion as observed by lipid and content mixing. *Biointerphases.* 3:FA17.

24. Scott, H. L., A. Skinkle, …, F. A. Heberle. 2019. On the mechanism of bilayer separation by extrusion, or why your LUVs are not really unilamellar. *Biophys. J.* 117:1381–1386.

25. van Lengerich, B., R. J. Rawle, …, S. G. Boxer. 2013. Individual vesicle fusion events mediated by lipid-anchored DNA. *Biophys. J.* 105:409–419.

26. Harris, A., G. Cardone, …, A. C. Steven. 2006. Influenza virus pleiomorphy characterized by cryoelectron tomography. *Proc. Natl. Acad. Sci. USA.* 103:19123–19127.

27. Nathan, L., and S. Daniel. 2019. Single virion tracking microscopy for the study of virus entry processes in live cells and biomimetic platforms. *Adv. Exp. Med. Biol.* 1215:13–43.

28. Zawada, K. E., D. Wrona, …, P. M. Kasson. 2016. Influenza viral membrane fusion is sensitive to sterol concentration but surprisingly robust to sterol chemical identity. *Sci. Rep.* 6:29842.

29. van der Borg, G., S. Braddock, …, W. H. Roos. 2018. Single-particle fusion of influenza viruses reveals complex interactions with target membranes. *J. Phys. Condens. Matter.* 30:204005.

30. Lozano, M. M., J. S. Hovis, …, S. G. Boxer. 2016. Dynamic reorganization and correlation among lipid raft components. *J. Am. Chem. Soc.* 138:9996–10001.

31. Pan, J., T. T. Mills, …, J. F. Nagle. 2008. Cholesterol perturbs lipid bilayers nonuniversally. *Phys. Rev. Lett.* 100:198103.

32. Aeffner, S., T. Reusch, …, T. Salditt. 2012. Energetics of stalk intermediates in membrane fusion are controlled by lipid composition. *Proc. Natl. Acad. Sci. USA.* 109:E1609–E1618.

33. Chernomordik, L. V., and M. M. Kozlov. 2008. Mechanics of membrane fusion. *Nat. Struct. Mol. Biol.* 15:675–683.

34. Chlanda, P., E. Mekhedov, …, J. Zimmerberg. 2016. The hemifusion structure induced by influenza virus haemagglutinin is determined by physical properties of the target membranes. *Nat. Microbiol.* 1:16050.

35. Kollmitzer, B., P. Heftberger, …, G. Pabst. 2013. Monolayer spontaneous curvature of raft-forming membrane lipids. *Soft Matter.* 9:10877–10884.

36. Patel, D. S., S. Park, …, W. Im. 2016. Influence of ganglioside GM1 concentration on lipid clustering and membrane properties and curvature. *Biophys. J.* 111:1987–1999.

37. van Gorkom, L. C., J. J. Cheetham, and R. M. Epand. 1995. Ganglioside GD1a generates domains of high curvature in phosphatidylethanolamine liposomes as determined by solid state 31P-NMR spectroscopy. *Chem. Phys. Lipids.* 76:103–108.

Biophysical Journal, Volume *118*

Supplemental Information

Target Membrane Cholesterol Modulates Single Influenza Virus Membrane Fusion Efficiency but Not Rate

Katherine N. Liu and Steven G. Boxer

I. Supplementary Methods

Flow cell and glass coverslip preparation. Polydimethylsiloxane (PDMS) flow cells were prepared and plasma bonded to glass coverslips, as previously described (1). Briefly, glass coverslips (24 x 40 mm, No 1.5, VWR International, Randor, PA) were cleaned by heating in 1:7 diluted 7X detergent in DI for 30 min, then rinsed extensively in DI water for 4 hours. Glass surfaces were annealed by baking slides in a kiln at 400˚C for 4 hours. PDMS flow cells (with channel dimensions 2.5 mm x 13 mm x 70 µm) and cleaned coverslips were plasma cleaned for at least 2 min and bonded together.

AF546-DNA-lipid preparation. AlexaFluor 546-labeled DNA-lipids were prepared by NHS coupling of AlexaFluor 546 succinimidyl ester to the DNA-lipid via a 3' amine as previously described (3).

Table S1. DNA-lipid sequences.

Name	DNA sequence (5'-3')	Location
A	Biotin-TTT TTT TTT TTT TTT TTT TTT TTT	Glass slide
A'	Lipid-AAA AAA AAA AAA AAA AAA AAA AAA	Influenza envelope
B	Lipid-CCC CCC CCC CCC CCC CCC CCC CCC CCC CCC CCC CCC CCC CCC CCC CCC CCC CCC CCC CCC CCC CCC CCC TCG ACA CGG AAA TGT TGA ATA CTA	Influenza envelope
B'	Lipid-TAG TAT TCA ACA TTT CCG TGT CGA	Target vesicle
X	Lipid-TGC GGA TAA CAA TTT CAC ACA GGA-AF546	Influenza envelope

Fluorescent labeling of influenza. For DNA-lipid quantification experiment only: Oregon Green-DHPE (OG-DHPE, 0.75 mg/mL in ethanol) was mixed with HB buffer in a 1:120 ratio. For virus dequenching experiments: Texas Red-DHPE (TR-DHPE, 0.75 mg/mL in ethanol) was mixed with HB buffer in a 1:40 ratio. 9 µL of influenza A virus (2 mg/mL) was mixed with 36 µL of OG-DHPE/HB buffer or TR-DHPE/HB buffer solution and incubated at RT for 2 hours while rocking to incorporate fluorescently-tagged lipids into IAV envelope. To separate unincorporated OG-DHPE or TR-DHPE from labeled virions, about 1.35 mL of HB buffer was added, and virus was pelleted by centrifugation at 21,130 rcf for 1 hour. The pellet containing labeled virions was resuspended in 50 µL of fresh HB buffer. DNA-lipids of sequence X (Table S1) were incorporated into influenza envelope by incubating virus sample at 4˚C on ice overnight according to previous method (1).

Additional microscopy information. Texas Red images were obtained using a Texas Red filter cube (ex = 562/40 nm, bs = 593 nm, em = 624/40 nm) and additional excitation (560/55 nm) and emission (645/75 nm) filters. All images and video micrographs were captured with a frame rate of 288 ms/frame.

Monolayer spontaneous curvature (SC) calculations: SC values of mixtures were calculated by taking the weighted average of the SC value for each individual component (4). The SC values used in the calculations are: POPC = 0.022 nm^{-1}, DOPE = -0.399 nm^{-1}, and cholesterol = -0.494 nm^{-1}. All vesicle mixtures also contained 7 mol% TR-DHPE. The receptor-containing vesicles all contained 2 mol% GD1a. The contributions of TR-DHPE and GD1a were omitted from these estimations as SC values are not available.

Table S2. Lipid monolayer spontaneous curvature (SC) values for various mixtures used in this study.

Cholesterol (mol%)	DOPE (mol%)	POPC (mol%)	TR-DHPE* (mol%)	Estimated monolayer spontaneous curvature (nm^{-1})
10	20	63	7	-0.143
20	20	53	7	-0.190
30	20	43	7	-0.237
40	20	33	7	-0.284

Values are based on individual SC values in the literature (see text and reference (4)). Other than cholesterol, mixtures contained 20 mol% DOPE, 7 mol% TR-DHPE, and remaining mol% POPC. Receptor-containing mixtures also contained 2 mol% GD1a. *TR-DHPE and GD1a were omitted from the SC calculation.

II. Supplementary Results

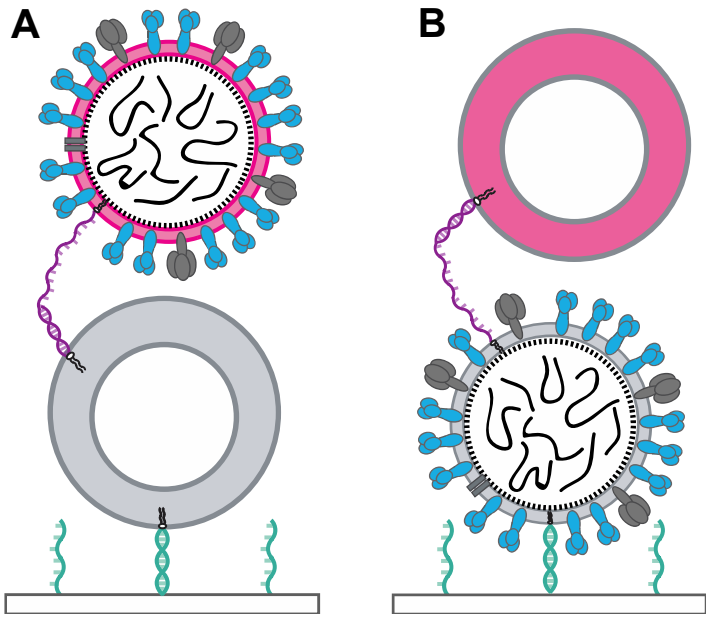

Figure S1. Schematic of single virus assay geometries.
(A) Lipid-labeled virus: In previous work, IAV lipid mixing was observed by introducing a self-quenched concentration of Texas Red-DHPE into the IAV envelope. In this architecture, virions were bound to target vesicles by hybridization of complementary sequences (Sequences B, B') of membrane-anchored DNA (purple). Vesicles were surface-tethered to the substrate through hybridization of an orthogonal sequence (Sequences A, A') of membrane-anchored DNA (green). Figure adapted from reference (1). (B) Lipid-labeled vesicle: In this study, IAV lipid mixing events are observed through dequenching of Texas Red lipid-labeled target vesicles (as shown in Fig. 1A). Surface passivation is especially important in this configuration to avoid non-specific binding of incoming vesicles (see Methods).

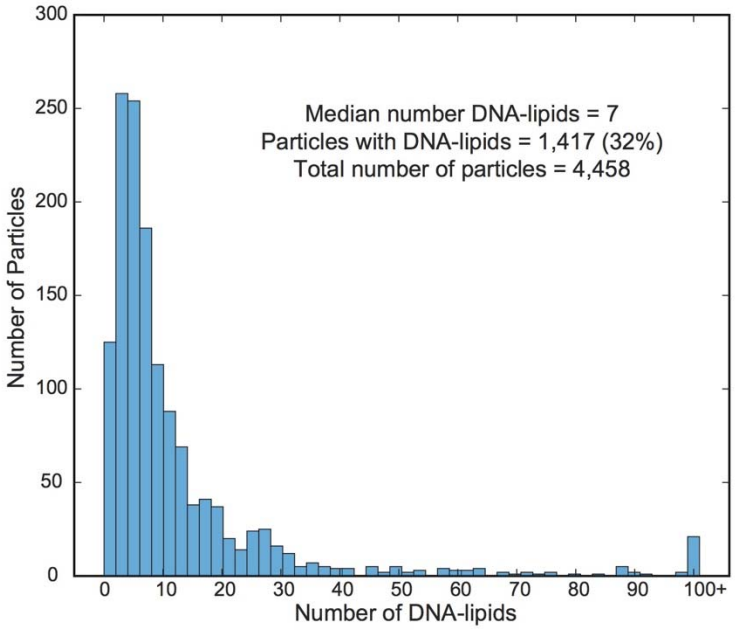

Figure S2. Distribution of DNA-lipid tether incorporation into influenza A virions that contain at least one DNA-lipid.

The DNA-lipid incorporation into virions was quantified by using an AlexaFluor-546 (AF546) labeled DNA-lipid (Sequence X, Table S1). The number of DNA-lipids in each virion was measured by quantitative fluorescence imaging, as done in previous work (1, 5, 6). Briefly, the average fluorescence intensity of one AF546 DNA-lipid was determined by single step photobleaching. AF546 DNA-lipids were incorporated into OG-DHPE labeled virions, which were non-specifically bound in a microfluidic flow cell to a glass coverslip. This is the only example of IAV fluorescent labeling in this study; all other experiments were performed with IAV that did not contain any fluorescent lipids. After the flow cell was thoroughly rinsed, virions were imaged in the Alexa 546 and OG-DHPE channels. The number of DNA-lipids were calculated by dividing the AF546 intensity of each virion by the average intensity per AF546 DNA-lipid. DNA-lipid incorporation into the IAV envelope does not follow Poisson statistics. 32% of virions contain at least one DNA-lipid, and of these, the median number of DNA-lipids incorporated is 7. The median number of DNA-lipids per virion is 200- to 350-fold fewer than the number of fluorescently tagged lipids added to the viral envelope in order to achieve a self-quenched concentration in alternate architectures. Total virions analyzed = 4,458.

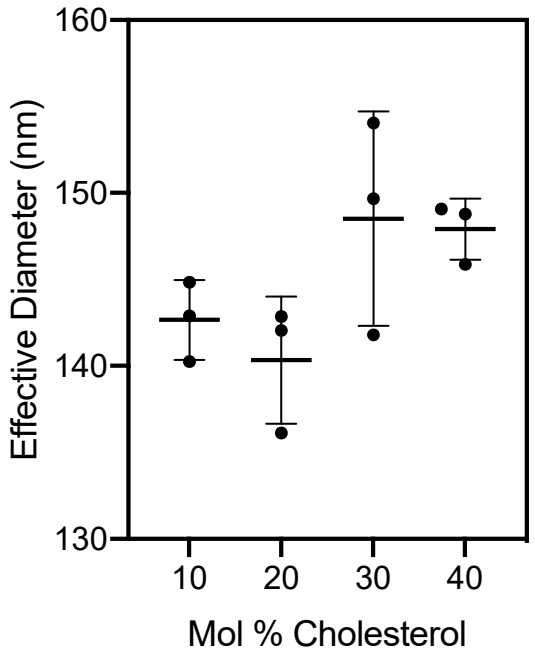

Figure S3. Diameter of vesicles as determined by dynamic light scattering (DLS).
Vesicles of lipid mixtures used in this study (see Table S2, no GD1a, no TR-DHPE) were prepared by extrusion through 100 nm polycarbonate membranes. Increasing the mol% cholesterol did not lead to a significant change in the size distribution of vesicles as determined by a one-way ANOVA ($p = 0.200$). Mean and standard deviation are shown from three independent experimental preparations. DLS measurements were performed in the Stanford Shared Nano Facilities.

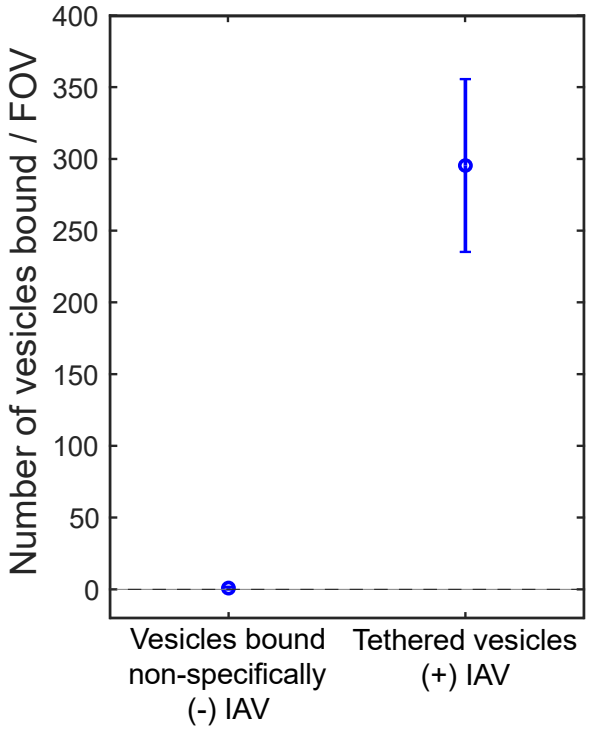

Figure S4. Minimal vesicle binding occurs in the absence of IAV.
In microfluidic flow cells, glass slides were functionalized with (left): PLL-g-PEG, PLL-g-PEG-biotin, and neutrAvidin, and (right): PLL-g-PEG, PLL-g-PEG-biotin, neutrAvidin, biotinylated DNA, IAV, and BSA (as described in Methods). Vesicles were subsequently introduced to both surface preparations, and after 25 min, excess vesicles were rinsed away with vesicle buffer. The number of vesicles were quantified per microscope field of view (FOV). Points represent average number of vesicles ± standard deviation. The composition of vesicles in these experiments was 10 mol% cholesterol, 20 mol% DOPE, 63 mol% POPC, and 7 mol% TR-DHPE. Vesicles also contained DNA-lipids with sequence B' (see Table S1).

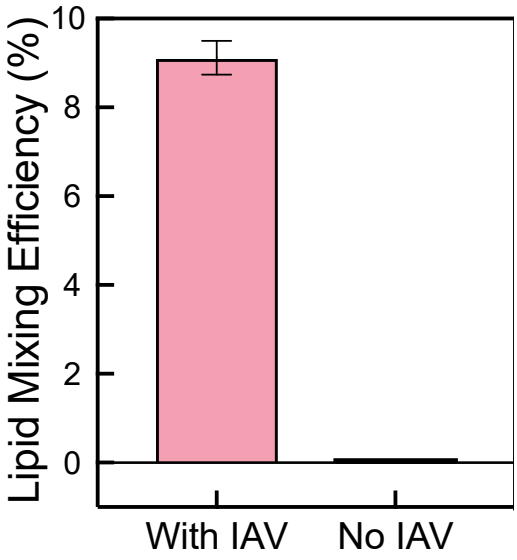

Figure S5. Vesicle dequenching occurs only at low pH when lipid-labeled target vesicles are tethered to influenza A virions. When lipid-labeled vesicles are DNA-tethered to the substrate (no IAV present in system) and the pH of the flow cell is lowered, there are no detectable vesicle dequenching events. In the presence of IAV, the efficiency, or the fraction of vesicles in one FOV that undergo lipid mixing, is 9.1%. The composition of vesicles in these experiments was 10 mol% cholesterol, 20 mol% DOPE, 61 mol% POPC, 2 mol% GD1a, 7 mol% TR-DHPE.

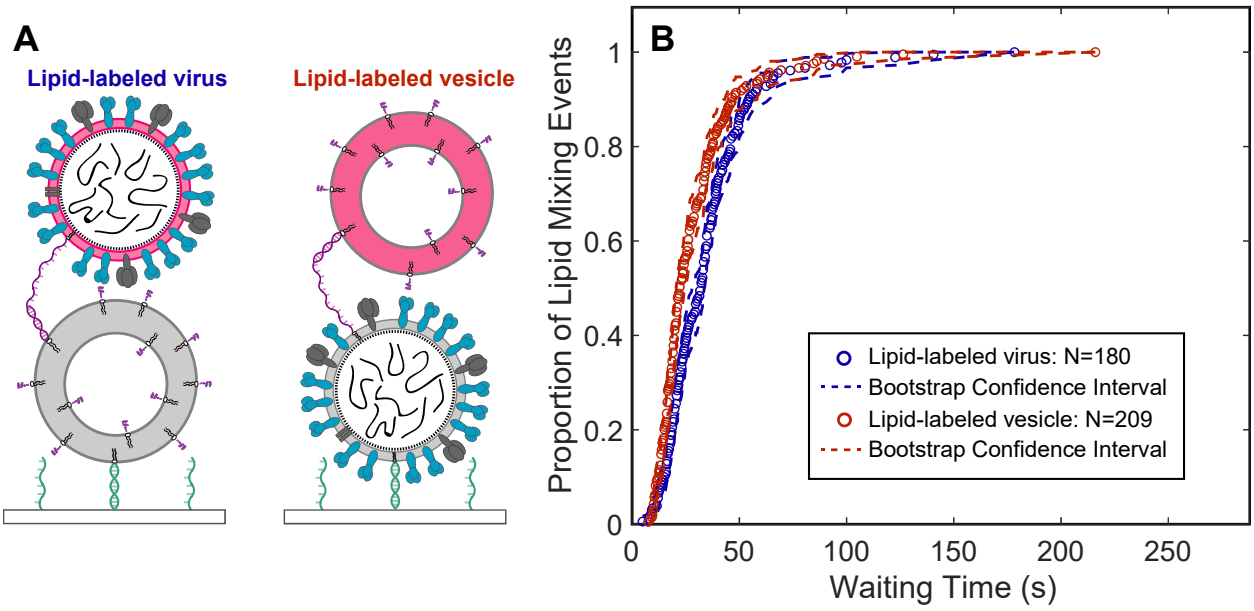

Figure S6. The rate of IAV lipid mixing for virions bound to target vesicles through GD1a and DNA-lipids is independent of surface-tethered geometry. (A) Schematic of lipid-labeled virus architecture (blue) and lipid-labeled vesicle architecture (red). The individual components of these architectures are described in detail in Fig. 1 and Fig. S1. (B) Wait times for individual lipid mixing events are plotted as a cumulative distribution function (CDF). For both assay geometries, the rate of IAV lipid mixing is the same within bootstrap resampling error (95% confidence intervals). The lipid mixing efficiencies were not significantly different within bootstrap resampling error. Lipid-labeled virus: 180/1452 particles, lipid-labeled vesicle: 209/2224 particles.

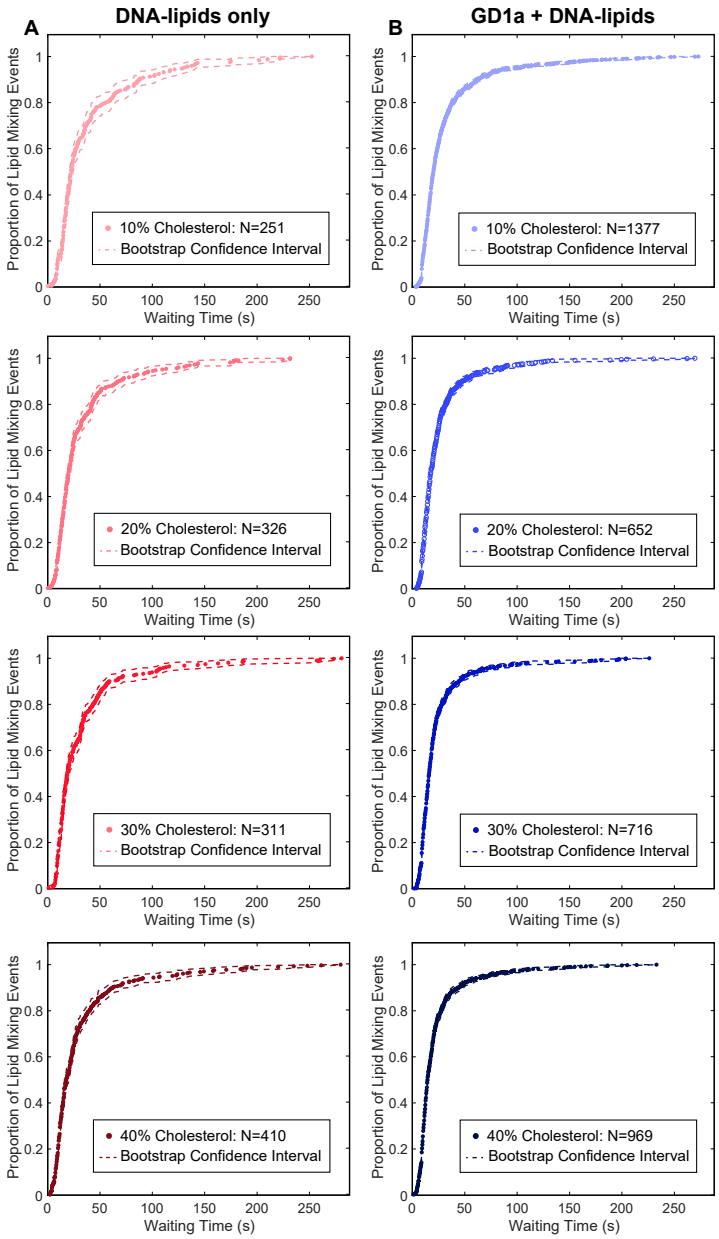

Figure S7. Individual CDFs for IAV lipid mixing to target vesicles containing various amounts of cholesterol.

Vesicles were tethered to virions through (A) DNA-lipids (red) or (B) DNA-lipids and GD1a (blue). Wait times for individual lipid mixing events are plotted as CDFs. Dashed lines represent bootstrap resampling error (95% confidence intervals). As the fraction of cholesterol (CH) increases, efficiency also increases ~4-fold: (A) 251/3939 particles for 10% CH, 326/3544 particles for 20% CH, 311/1858 for 30% CH, 410/1865 particles for 40% CH. (B) 1377/15099 particles for 10% CH, 652/3448 particles for 20% CH, 716/2401 for 30% CH, 969/2495 particles for 40% CH. The total number of vesicles analyzed is proportional to the number of individual experiments executed, and not due to inherent differences in tethering behavior.

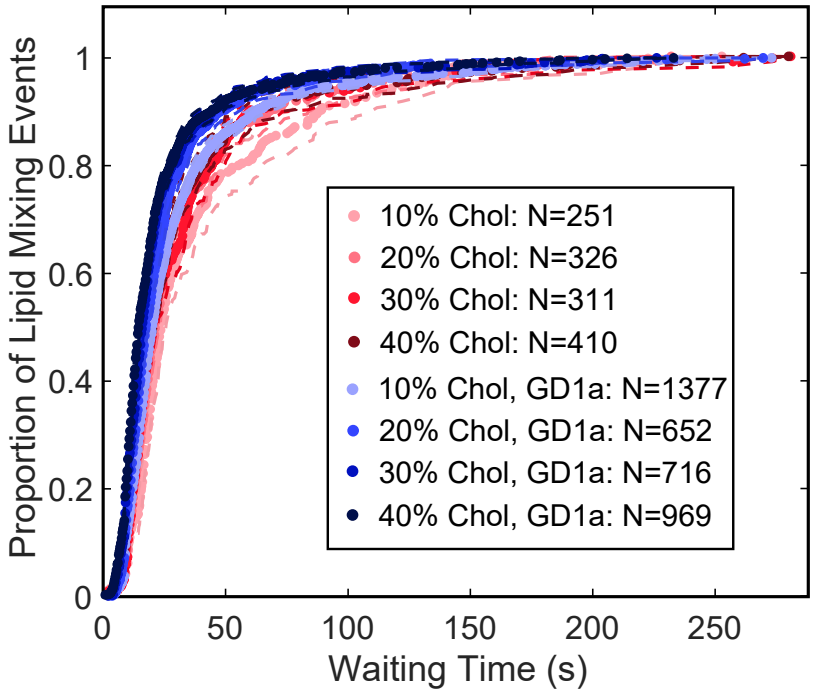

Figure S8. The rates of lipid mixing in the presence and absence of GD1a are not significantly different.

As in Fig. S7, vesicles were tethered to virions through DNA-lipids (red) or DNA-lipids and GD1a (blue). Wait times for individual lipid mixing events are plotted as CDFs. Dashed lines represent bootstrap resampling error (95% confidence intervals).

III. References

1. Rawle, R.J., S.G. Boxer, and P.M. Kasson. 2016. Disentangling Viral Membrane Fusion from Receptor Binding Using Synthetic DNA-Lipid Conjugates. Biophys. J. 111: 123–131.
2. Scott, H.L., A. Skinkle, E.G. Kelley, M.N. Waxham, I. Levental, and F.A. Heberle. 2019. On the Mechanism of Bilayer Separation by Extrusion, or Why Your LUVs Are Not Really Unilamellar. Biophys. J. 117: 1381–1386.
3. Van Lengerich, B., R.J. Rawle, P.M. Bendix, and S.G. Boxer. 2013. Individual vesicle fusion events mediated by lipid-anchored DNA. Biophys. J. 105: 409–419.
4. Kollmitzer, B., P. Heftberger, M. Rappolt, and G. Pabst. 2013. Monolayer spontaneous curvature of raft-forming membrane lipids. Soft Matter. 9: 10877–10884.
5. Chan, Y.-H.M., B. van Lengerich, and S.G. Boxer. 2008. Lipid-anchored DNA mediates vesicle fusion as observed by lipid and content mixing. Biointerphases. 3: FA17–FA21.
6. Rawle, R.J., E.R. Webster, M. Jelen, P.M. Kasson, and S.G. Boxer. 2018. pH Dependence of Zika Membrane Fusion Kinetics Reveals an Off-Pathway State. ACS Cent. Sci. 4: 1503–1510.